CLASSIFICATION AND IMAGING OF SPENT NUCLEAR FUEL DRY CASKS USING COSMIC RAY MUONS

S. Chatzidakis, P. A. Hausladen, S. Croft, J. A. Chapman, J. J. Jarrell, J. M. Scaglione
Oak Ridge National Laboratory
1 Bethel Valley Road, Oak Ridge, TN 37831
chatzidakiss@ornl.gov

C.K. Choi, L.H. Tsoukalas
Department of Nuclear Engineering
Purdue University
400 Central Drive, West Lafayette, IN 47909
choi@purdue.edu; tsoukala@purdue.edu

ABSTRACT

The present work explores alternative approaches for in situ monitoring with near real-time data analysis and imaging of dry casks using muons. Monitoring can provide useful signals about the cask contents in a yes/no decision format faster and with fewer muons than traditional imaging. Imaging can be performed as a second step in this process if specific information about the location of the fuel assemblies is needed. To explore and analyze these two modalities, simulations of muon scattering and displacement were performed for various scenarios, including vertical and horizontal fully loaded dry casks, half-loaded dry casks, dry casks with one row of fuel assemblies missing, dry casks with one fuel assembly missing, and empty dry casks. This work demonstrates monitoring can provide fast and reliable indication about the contents of the cask. For 100,000 muons, a few minutes of measurement time with a 3.6 m^2 detector at a 45° zenith angle, 90% detection probability for missing fuel assemblies can be achieved with a false alarm rate lower than 1%. If a positive signal is detected, then longer measurements can be performed and coupled with muon imaging algorithms to determine the location of missing nuclear material. In these cases, transmission muon radiography can produce images of acceptable resolution for all scenarios. In the horizontal dry cask case, all scenarios can be identified and separated adequately. In the vertical dry cask case, similar conclusions can be drawn, but because of shadowing from other fuel assemblies, the location of a missing fuel assembly cannot be identified in the 2-D transmission map. However, views from different directions may resolve this.

Key Words: Muons, Imaging, Classification, Dry Casks

1 INTRODUCTION

During the long service life of dry storage casks containing spent nuclear fuel, intermediate handling and transportation activities take place that create long-term fuel integrity performance questions. In addition, each dry cask contains significant quantities of plutonium that could be weaponized if retrieved. Through its safeguards program, the International Atomic Energy Agency (IAEA) has established criteria to verify nuclear material is not diverted from peaceful applications [1]. The rapid expansion of dry storage facilities and the safeguards requirement to maintain continuity of knowledge calls for innovative technologies to fill this critical gap.

Dry casks are heavily shielded (~1.5–2 m thick concrete or steel), and conventional methods for examining the interior are limited. For example, 1–10 MeV γ-rays have an attenuation coefficient approximately in the order of 25 g/cm^2, which results in less than 20 cm penetration in lead and 100 cm in

concrete [2]. Increasing the photon energy does not increase the penetrating distance because of the increase in pair production [3]. Similarly, electrons cannot penetrate far into matter because of large momentum transfers and radiation emission (i.e., Bremsstrahlung). For example, 1 GeV electrons can only penetrate water 1 m, and from a practical standpoint, available portable Betatrons can generate electrons with energies less than 10 MeV. Production of high-energy protons requires large, expensive, and immovable accelerators. Cosmic ray muons present certain advantages over the ionizing radiation. Muons can penetrate high-density materials, and their range increases with increasing energy. Fig. 1 shows the range of 1 GeV muons as a function of the atomic number compared with other types of radiation. Even in dense materials such as uranium and lead, muons have the deepest penetrating capabilities. In addition, muons are freely available, and no radiological sources are required eliminating any artificial radiological dose.

Past efforts have mainly focused on the use of muons for cargo scanning applications and proof-of-principle studies [4–7] and only recently focus has shifted to the point of imaging dry casks [8–15]. For cask imaging purposes, muon attenuation and scattering has several advantages over traditional methods, and muon imaging particularly well suited for large containers storing unknown materials with limited access [3]. Thomay et al. (2016) used muon scattering tomography to obtain 3-D images of the contents of legacy nuclear waste drums [8]. High and low density materials enclosed in concrete were resolved. For example, a small tungsten cylinder and a thin uranium sheet were identified. A notable example is the experimental effort by Durham et al. (2016) that used a small muon detector, the Mini Muon Tracker, to identify missing pressurized water reactor fuel bundles in a sealed vertical dry cask [9]. They performed measurements on a partially loaded vertical dry storage cask and could reconstruct 2-D images of areal density. They could locate columns of missing fuel bundles but not pinpoint their exact location.

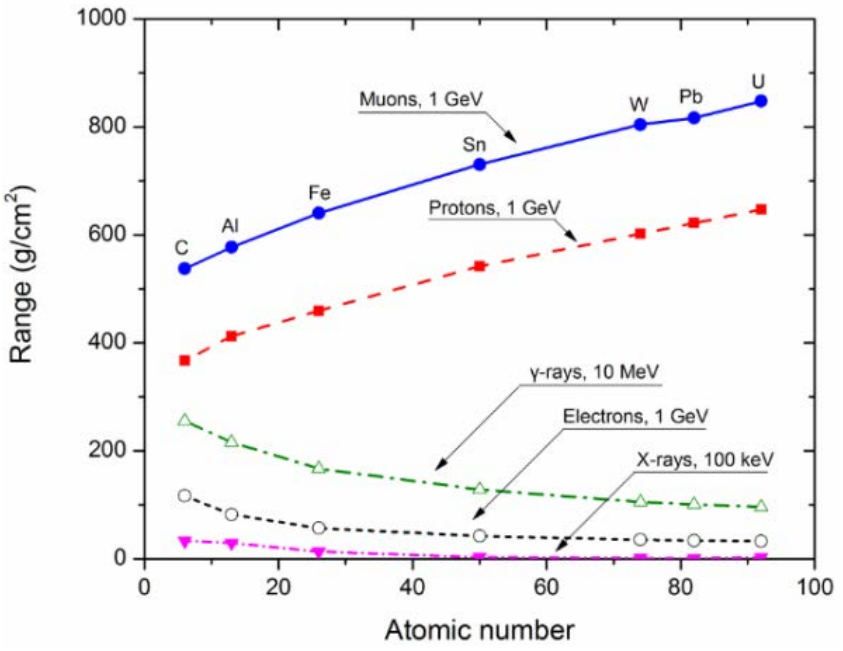

Figure 1. Range (mass density units) of various radiation types in various materials.

The present work explores alternative approaches for in situ monitoring with near real-time data analysis and imaging of dry casks using muons. Monitoring can provide useful signals about the cask contents in a yes/no decision format faster and with fewer muons than traditional imaging. Imaging can be performed as a second step in this process if specific information about the location of the fuel assemblies is needed. To explore and analyze these two modalities, simulations of muon scattering and

displacement were performed for various scenarios, including vertical and horizontal fully loaded dry casks, half-loaded dry casks, dry casks with one row of fuel assemblies missing, dry casks with one fuel assembly missing, and empty dry casks. This work demonstrates monitoring can provide fast and reliable indication about the contents of the cask. For 100,000 muons, a few minutes of measurement time with a 3.6 m^2 detector at a 45° zenith angle, 90% detection probability for missing fuel assemblies can be achieved with a false alarm rate lower than 1%. If a positive signal is detected, then longer measurements can be performed and coupled with muon imaging algorithms to determine the location of missing nuclear material. In these cases, transmission muon radiography can produce images of acceptable resolution for all scenarios. In the horizontal dry cask case, all scenarios can be identified and separated adequately. In the vertical dry cask case, similar conclusions can be drawn, but because of shadowing from other fuel assemblies, the location of a missing fuel assembly cannot be identified in the 2-D transmission map. However, views from different directions may resolve this.

2 METHODOLOGY

The GEANT4 (GEometry ANd Tracking) Monte Carlo code [10] was used to perform muon–dry cask simulations and estimate muon paths through spent nuclear fuel dry casks. The methodology developed is shown in Fig. 2. Dry cask geometry, materials, muon energy, and angular distributions are needed to accurately reproduce the muon–dry cask interactions. Muon detection requires placement of detectors on opposite sides of the object that is to be inspected. Cosmic ray muons pass through the first detector plane, and their initial trajectories are recorded. The muons then pass through concrete and fuel (UO_2), exiting through another layer of concrete before hitting and interacting with the second plane of the detector, where their final trajectories are also recorded. The detectors are idealized gas chambers with 100% efficiency. To generate muons from the actual, measured muon spectrum, a cosmic ray muon sampling capability called the "muon event generator," was developed [11]. The muon event generator is based on a phenomenological model that captures the main characteristics of the experimentally measured spectrum, which is then coupled with a set of statistical algorithms. The muons generated can have zenith angles in the range 0°–90° and energies in the range 1–100 GeV. The muon angular and energy distributions are reproduced using the muon generator and integrated into GEANT4. Using this information, calculations were performed to determine where the muon interactions occurred, to determine their displacement and scattering angles, and to evaluate pattern classification and imaging algorithms. The orientation of the cask and the cask-to-cask interactions that may occur in an actual storage pad are not simulated.

3 DRY CASK CLASSIFICATION

Before muon imaging takes place, a binary classification can be made to determine if the cask is fully loaded or not. Since the muon scattering variance distributions are adequately separated between a fully loaded cask and one with a missing fuel assembly, a decision boundary can be drawn that makes the classification of different spent nuclear fuel dry casks feasible [11–14]. Given a binary classifier, there are four possible outcomes. If the true class is H_0 (for example an intact dry cask) and classified as H_0, then it is counted as true negative; if it is classified as H_1 (for example, missing fuel assembly), then it is counted as a false alarm (false positive). If the true class is H_1 and classified as H_0, then it is counted as a miss (false negative); if it is classified as H_1, then it is counted as detection (true positive). Given the measurements Y and the cost function C(δ(Y)), equation (1) shows the overall Bayesian risk, which is defined as the expectation of the cost of selecting class δ:

$$\mathrm{R}(\delta) = \mathbb{E}_{Y\Theta}[C(\delta(\boldsymbol{Y}), \Theta)]\,, \tag{1}$$

where Θ is the true decision. We seek to find a decision rule that will minimize the risk using the following equation (2):

$$\delta(y) = \underset{\delta}{\operatorname{argmin}}\, R(\delta)\,. \tag{2}$$

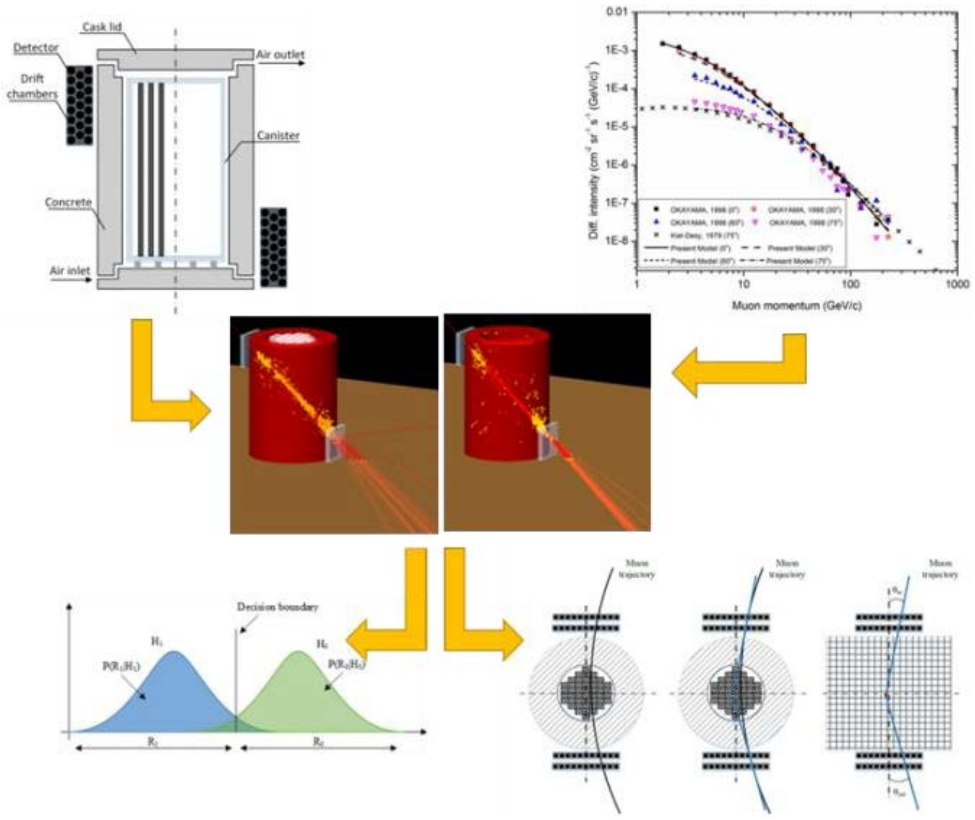

Figure 2. GEANT4 model of a vertical fully loaded and empty dry cask (*center*), scattering variance distributions (*bottom left*) and muon path through a cask (*bottom right*).

For uniform cost, the risk is simplified to the probability of error shows in equation (3):

$$\mathrm{R}(\delta) = \pi_0 \mathbb{P}(\mathcal{R}_1|\mathrm{H}_0) + \pi_1 \mathbb{P}(\mathcal{R}_0|\mathrm{H}_1) = \pi_0 \mathbb{P}_F + \pi_1 \mathbb{P}_M = \mathbb{P}_{error}\,, \tag{3}$$

where P_F and $P_M = 1 - P_D$ are the probability of false alarm and miss, and π_0 and π_1 are the prior probabilities for class H_0 and class H_1, respectively. This demonstrates the overall risk can be written as a function of the pair (P_F, P_D). Each muon measurement is described approximately as a Gaussian distribution of zero mean and variance σ^2. After substituting the probabilities and further rearranging, equation (4) is applied:

$$\frac{1}{N}\sum_{i=1}^{N} y_i^2 \underset{H_1}{\overset{H_0}{\lessgtr}} \frac{2\sigma_1^2\sigma_0^2}{(\sigma_1^2-\sigma_0^2)}\left[\ln\frac{\sigma_1}{\sigma_0}+\frac{\ln\tau}{N}\right], \tag{4}$$

where N is the number of muons, and τ is a parameter that depends on the priors and the cost function. A classifier using the above decision rule is an optimal classifier, which has a separation boundary (Fig. 3) that can be written as the sum of two terms. The first term depends solely on the characteristics of the scattering distribution, whereas the second term depends on the number of measurements, the priors, and the associated cost for each classification decision.

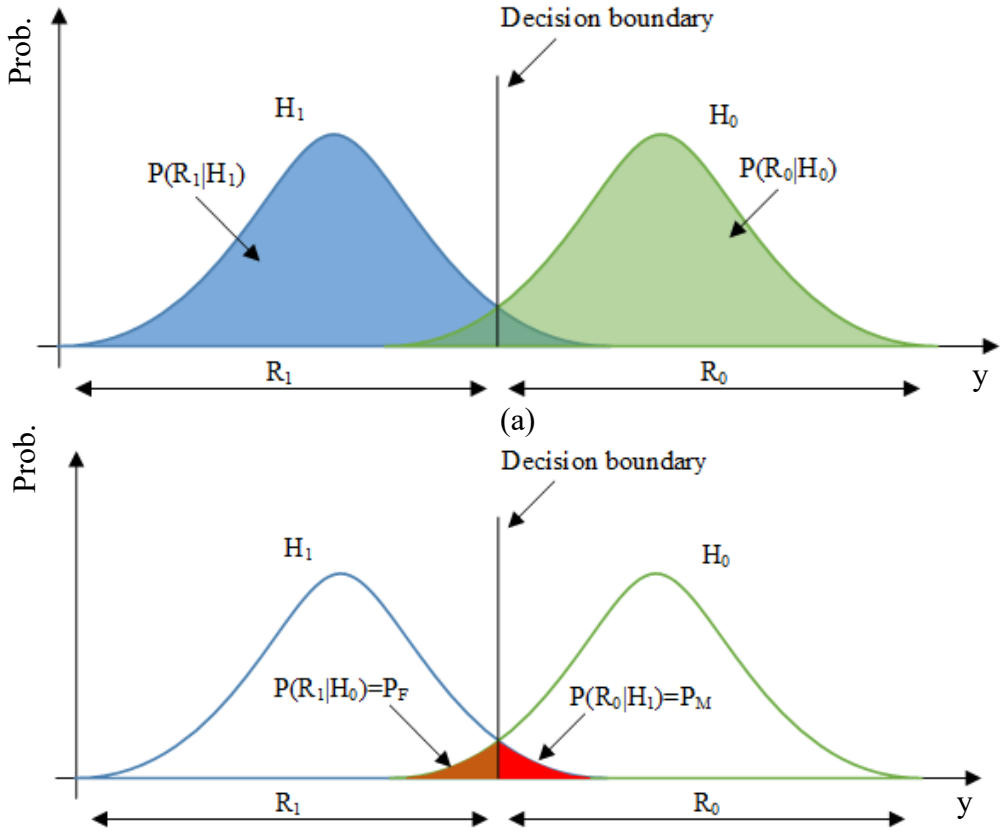

Figure 3. Probability distributions of two classes H_0 and H_1 and the decision boundary that separates the 1-D space in two sets R_0 and R_1 (*top*). The corresponding miss (red) and false alarm (orange) probabilities are also shown (*bottom*).

The structure of the Bayesian algorithm relies on adequate knowledge of priors and of the cost function. When this knowledge is not readily available, instead of guessing, we could select the threshold that will maximize the detection rate and keep the false alarm rate below a preselected value. Since the Bayesian risk is parametrized by the pair (P_D, P_F), it would be desirable to select a decision boundary where P_D is as close to 1 (or 100%) as possible, and P_F as close to zero as possible. To obtain the receiver operating characteristic (ROC) curve, the decision boundary τ is varied from +∞ to 0. Each location of the decision boundary generates a different pair (P_D, P_F). The decision boundary of +∞ produces the point (0,

0). As the boundary is further reduced, the curve moves up and to the right ending up at the point (1, 1). Fig. 4 shows ROC curves for 10,000, 50,000, and 100,000 muons and the corresponding decision boundaries for uniform cost. If an acceptable false alarm rate is less than10%, then the maximum detection rate that can be achieved is ~90%. Increasing muon measurements results in smaller false alarm rates and improved detection performance. For N = 100,000, a maximum detection rate of 90% can be achieved for a false alarm rate lower than 1%.

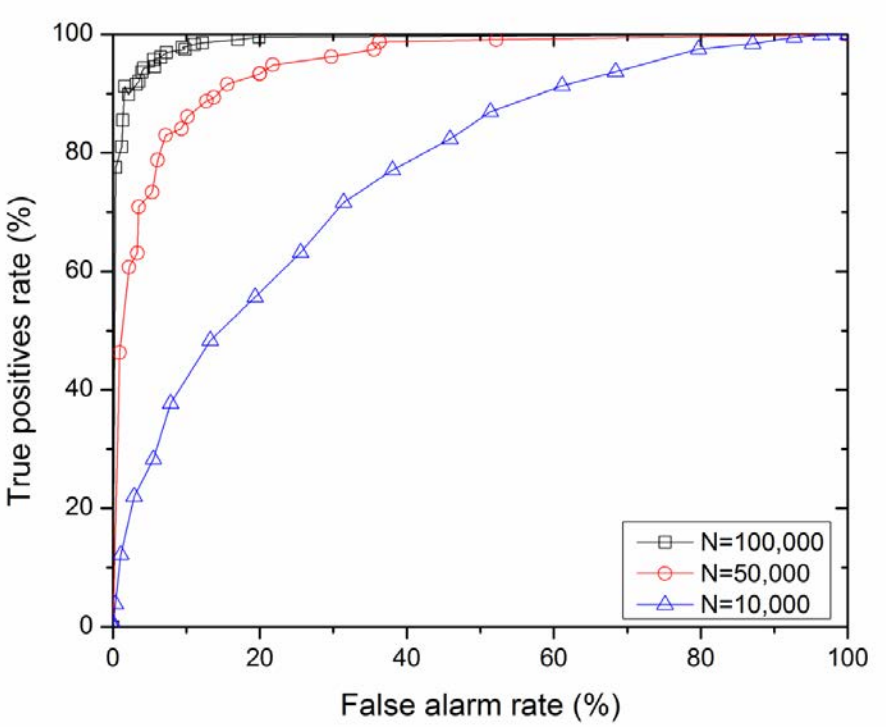

Figure 4. ROC curve for 50,000 muons. The threshold values τ are also shown.

4 DRY CASK IMAGING

Measuring the number of muons entering and the number of muons exiting a dry cask, 2-D flux maps showing density variations and 3-D scattering density maps can be produced. To produce a 2-D flux map, the scattering angles of incoming and outgoing muons were calculated, and only muons having scattering angles between $-10 \leq \theta \leq 10$ mrad were considered. These muons have been only slightly scattered and can be used as a parallel beam to produce a 2-D map similar to x-ray radiography. Muons passing through less dense materials (i.e., concrete) will have higher counts than muons passing through fuel assemblies. Two-dimensional maps were produced based on the simulation of 10^6 muons for a 3.6×3.6 m^2 detector and the following vertical and horizontal dry cask scenarios: (a) fully loaded, (b) half loaded, (c) row of fuel assemblies missing, (d) one fuel assembly missing, and (e) empty. The 2-D transmission maps shown in Figs. 5–6, are compared to the reconstruction using the Point of Closest Approach (PoCA) algorithm [15]. In the horizontal dry cask case, all scenarios can be immediately identified and adequately separated. Except for the missing fuel assembly, similar conclusions can be drawn in the vertical dry cask case. Because of shadowing from other fuel assemblies, the location of a missing fuel assembly cannot be identified in the 2-D transmission map. Although, the PoCA algorithm can provide a 3-D representation of the cask details, the 2-D maps outperform them, allowing the position of the assemblies to be identified. Figures 7–8 show the number of muons measured along the centerline of a dry cask compared with a fully loaded cask. A cask with a missing fuel assembly has a stronger signal than a fully loaded

cask; although, the signal-to-noise ratio is not high. Increasing the number of muons will increase the signal-to-noise ratio and will result in improved separation between the two cases.

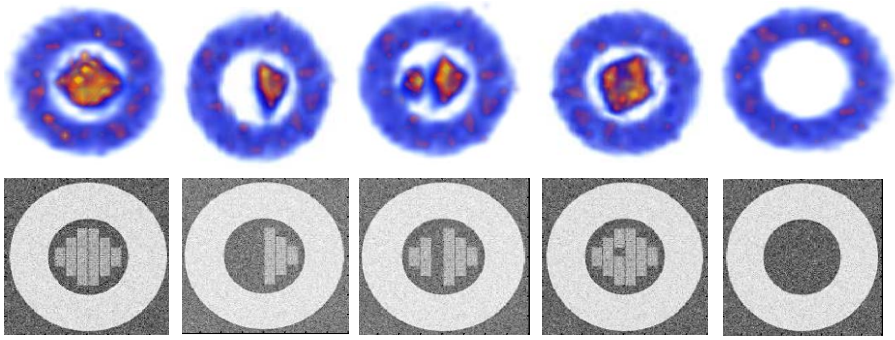

Figure 5. Comparison between PoCA (*top*) and muon transmission (*bottom*) for horizontal dry casks. From left to right: fully loaded, half loaded, row of fuel assemblies missing, one fuel assembly missing, and empty.

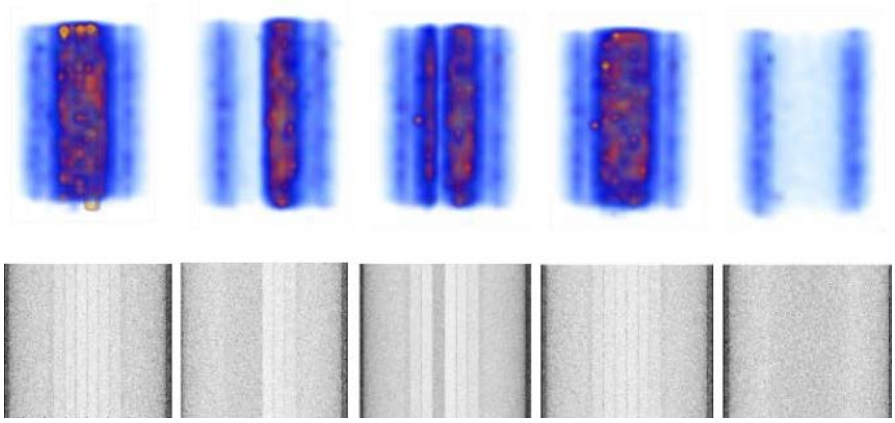

Figure 6. Comparison between PoCA (*top*) and muon transmission (*bottom*) for vertical dry casks. From left to right: fully loaded, half loaded, row of fuel assemblies missing, one fuel assembly missing, and empty.

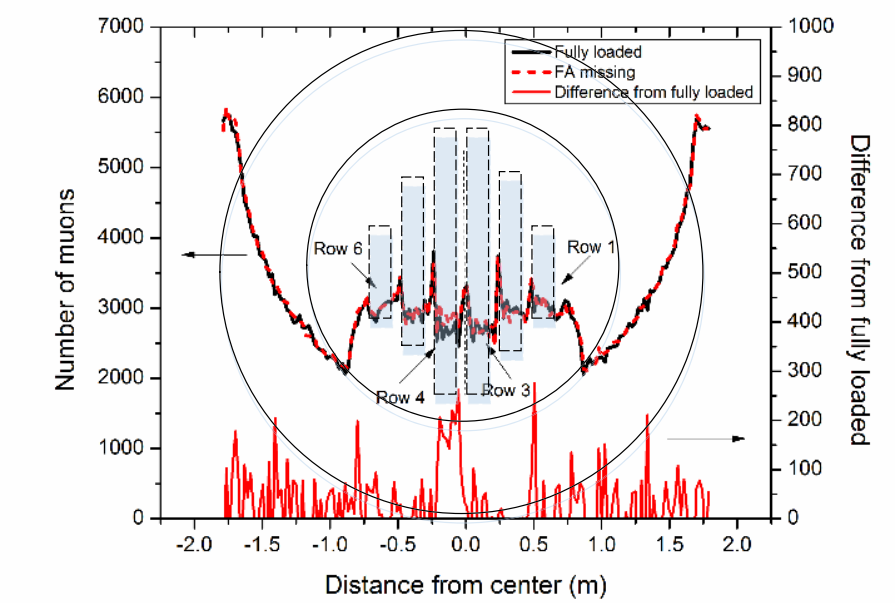

Figure 7. Number of muons measured along the centerline of a horizontal dry cask. Comparison with a fully loaded cask is included. The location of fuel assemblies is shown with thin dark gray lines.

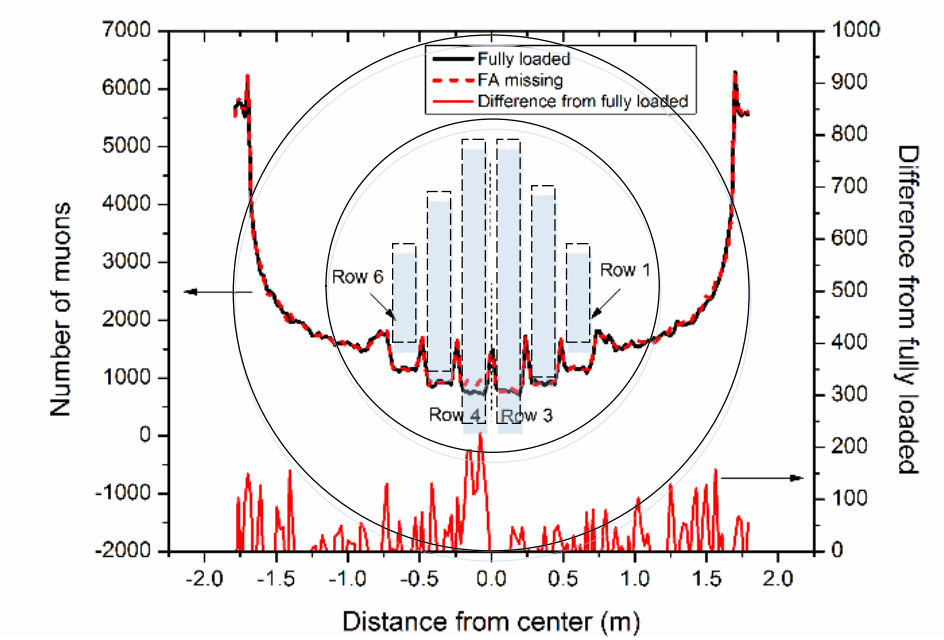

Figure 8. Number of muons measured along the centerline of a vertical dry cask. Comparison with a fully loaded cask is included. The location of fuel assemblies is shown with thin dark gray lines.

5 ACKNOWLEDGMENTS

Research sponsored by the Laboratory Directed Research and Development Program of Oak Ridge National Laboratory, managed by UT-Battelle, LLC, for the US Department of Energy.

6 REFERENCES

1. IAEA, "Design Measures to Facilitate Implementation of Safeguards at Future Water Cooled Nuclear Power Plants," Tech. Report Series No. 392, Vienna (1998).

2. K. Borozdin et al., "Radiographic Imaging with Cosmic Ray Muons," *Nature,* **Vol. 422**, p. 22 (2003).

3. P. M. Jenneson, "Large Vessel Imaging Using Cosmic Ray Muons," *Nucl. Instr. Methods Phys. Res. A,* **Vol. 525**, pp. 346–51 (2004).

4. L. J. Schultz et al., "Statistical Reconstruction of Cosmic Ray Muon Tomography," *IEEE Trans. Im. Proc.*, **Vol. 16**, pp. 1985–1993 (2007).

5. C. L. Morris et al., "Tomographic Imaging with Cosmic Ray Muons," *Science and Global Security,* vol. 16, Issue 1–2, pp. 37–53 (2008).

6. S. Pesente et al., "First Results on Material Identification and Imaging with a Large-Volume Muon Tomography Prototype," *Nuclear. Instr. Methods. Phys. Res. A,* **Vol. 604**, pp. 738–46 (2009).

7. L. J. Schultz et al., "Image Reconstructions and Material Z Discrimination Via Cosmic Ray Muon Radiography," *Nuclear Instruments and Methods in Physics Research A*, **Vol. 519**, pp. 687–94 (2004).

8. C. Thomay et al., "Passive 3D imaging of nuclear waste containers with muon scattering tomography," *J. Inst.,* **Vol. 11**, P03008 (2016).

9. J. M. Durham et al., "Cosmic Ray Muon Imaging of Spent Nuclear Fuel in Dry Storage Casks," *J. Nuc. Mat. Manag.,* **Vol. 44**, p. 3 (2016).

10. S. Agostinelli et al., "GEANT4—A Simulation Toolkit," *Nuclear Instruments and Methods in Physics Research A*, **Vol. 506**, pp. 250–303 (2003).

11. S. Chatzidakis et al., "Developing A Cosmic Ray Muon Sampling Capability for Muon Tomography and Monitoring Applications," *Nuclear Instruments and Methods in Physics Research A*, **Vol. 804**, pp. 33–42 (2015).

12. S. Chatzidakis et al., "A Bayesian Approach to Monitoring Spent Fuel Using Cosmic Ray Muons," *Trans. Am. Nucl. Soc.*, **Vol. 111**, pp. 369–70 (2014).

13. S. Chatzidakis et al., "Monte-Carlo Simulations of Cosmic Ray Muons for Dry Cask Monitoring," *Trans. Am. Nucl. Soc.*, **Vol. 112**, pp. 534–36 (2015).

14. S. Chatzidakis et al., "Interaction of Cosmic Ray Muons with Spent Nuclear Fuel Dry Casks and Determination of Lower Detection Limit," *Nucl. Instr. Methods Phys. Res. A,* **Vol. 828**, pp. 37–45 (2016).

15. S. Chatzidakis et al., "Analysis of Spent Nuclear Fuel Imaging Using Multiple Coulomb Scattering of Cosmic Muons," *IEEE Trans. Nuc. Sci.*, **Vol. 63**, p. 2866 (2016).